inverted V's are associated with boundary regions between open and closed field lines. The precipitation of electrons and the corresponding acceleration and escape of ionospheric ions take place in clefts interfacing magnetic anomalies and in the boundary interfacing the large-scale magnetization region with the nonmagnetized region at Mars.

Results from ASPERA-3 on MEX (*20*) suggest that energization and outflow of plasma may initiate at fairly low altitudes. Similarly, the nightside energization and outflow may also reach down to low altitudes, perhaps even lower in view of the low nightside ionization. The observations of upward-accelerated ions combined with downward-accelerated electrons are observed on flux tubes that are semi-open or open, connecting to strong crustal magnetizations. However, we also observe acceleration in boundaries enclosing the large-scale regions of crustal magnetization. The intense fluxes of upgoing ionospheric ions represent the erosion of ionospheric plasma and the formation of plasma density cavities (*21*). A combination of parallel electric fields and waves deepens the cavities and promotes an acceleration process in which parallel acceleration and heating are strongly coupled. This is consistent with the linear relation found between the ion peak/beam energy and the beam temperature (Fig. 3, left), as previously observed above terrestrial discrete auroras associated with field-aligned plasma acceleration (*5*).

Discrete auroras are therefore expected to occur in clefts interfacing with strong crustal magnetization regions at Mars (Fig. 5), but also in the interface region connecting the void and presence of crustal magnetizations at Mars. To complete the analogy between terrestrial discrete auroras and martian auroras, the precipitating energy flux of electrons Θ_a is derived by adding the local energy flux Θ_i and the energy flux gained by electron acceleration P_a down to the atmosphere. P_a is computed using the acceleration voltage (V_0) inferred from upgoing ionospheric ion beams (Fig. 3, left). For electrostatic acceleration along a unit magnetic flux tube, assuming acceleration in a narrow altitude range, the total energy flux gain is given by $P_a \approx eV_0\Phi_i$, where Φ_i represents the local downward electron flux. Thus $\Theta_a \approx \Theta_i + eV_0\Phi_i$. From 17 inverted V's, we obtain the local maximum energy flux Θ_i = 0.01 to 3 mW/m^2, from which we derive Θ_a = 1 to 50 mW/m^2. The latter corresponds to 2- to 80-kilorayleigh visible emissions (at 557.7 nm; the "green line") above Earth. In a similar manner, the density distribution of atomic oxygen from a time-averaged model of the martian atmosphere (*22*) suggests that the green-line aurora is generated above magnetic cusps and clefts in the nightside of Mars at atmospheric heights of 50 to 80 km.

References and Notes

1. C. E. MacIlwain, *J. Geophys. Res.* **65**, 2727 (1961).
2. R. D. Albert, *Phys. Rev. Lett.* **18**, 368 (1967).
3. L. A. Frank, K. L. Ackerson, *J. Geophys. Res.* **76**, 3612 (1971).
4. E. G. Shelley, R. G. Johnson, R. D. Sharp, *Geophys. Res. Lett.* **3**, 654 (1976).
5. T. E. Moore *et al.*, *Space Sci. Rev.* **88**, 7 (1999).
6. R. Lundin *et al.*, *Nature* **341**, 609 (1989).
7. H. Pérez-de Tejada, *J. Geophys. Res.* **92**, 4713 (1987).
8. J. G. Luhmann, S. J. Bauer, *AGU Monogr.*, **66**, 417 (1992).
9. M. J. Acuña *et al.*, *Science* **284**, 790 (1999).
10. A. M. Krymskii *et al.*, *J. Geophys. Res.* **107** (A9), 1245 (2002).
11. D. L. Mitchell *et al.*, *J. Geophys. Res.* **106**, 23419 (2001).
12. J.-L. Bertaux *et al.*, *Nature* **435**, 9 (2005).
13. S. Barabash *et al.*, in *Mars Express: The Scientific Payload* (ESA SP-1240, European Space Agency, Noordwijk, Netherlands, 2004), pp. 121–139.
14. W. B. Hanson *et al.*, *J. Geophys. Res.* **82**, 4351 (1977).
15. D. S. Evans, *J. Geophys. Res.* **79**, 2853 (1974).
16. Y. T. Chiu, M. Schulz, *J. Geophys. Res.* **83**, 629 (1978).
17. R. D. Sharp, R. G. Johnson, E. G. Shelley, *J. Geophys. Res.* **82**, 3324 (1977).
18. J. D. Winningham *et al.*, *Icarus,* in press.
19. R. Lundin *et al.*, *Icarus,* in press.
20. R. Lundin *et al.*, *Science* **305**, 1933 (2004).
21. W. Calvert, *Geophys. Res. Lett.* **8**, 919 (1981).
22. M. B. McElroy *et al.*, *J. Geophys. Res.* **82**, 4379 (1977).

23. ASPERA-3 on the European Space Agency's (ESA's) MEX is a joint effort between 15 laboratories in 10 countries. We are indebted to the national agencies supporting ASPERA-3 and to ESA for making MEX a great success.

31 October 2005; accepted 5 January 2006
10.1126/science.1122071

Dissociation of $MgSiO_3$ in the Cores of Gas Giants and Terrestrial Exoplanets

Koichiro Umemoto,[1] Renata M. Wentzcovitch,[1]* Philip B. Allen[2]

$CaIrO_3$-type $MgSiO_3$ is the planet-forming silicate stable at pressures and temperatures beyond those of Earth's core-mantle boundary. First-principles quasiharmonic free-energy computations show that this mineral should dissociate into CsCl-type MgO + cotunnite-type SiO_2 at pressures and temperatures expected to occur in the cores of the gas giants and in terrestrial exoplanets. At ~10 megabars and ~10,000 kelvin, cotunnite-type SiO_2 should have thermally activated electron carriers and thus electrical conductivity close to metallic values. Electrons will give a large contribution to thermal conductivity, and electronic damping will suppress radiative heat transport.

The transformation of $MgSiO_3$-perovskite into the $CaIrO_3$-type structure near Earth's core-mantle boundary (CMB) conditions (*1–3*) invites a new question: What is the next polymorph of $MgSiO_3$? The importance of this question has increased since the discoveries of two new exoplanets: the Earth-like planet with ~7 Earth masses (*4*) (Super-Earth hereafter) and the Saturn-like planet with a massive dense core with ~67 Earth masses (*5*) (Dense-Saturn hereafter). The extreme conditions at the giants' cores (*6*) and exoplanet interiors are challenging for first-principles methods. Electrons are thermally excited, and core electrons start to participate in chemical bonds. This requires either all-electron methods or the development of pseudopotentials based on core orbitals. Neither density functional theory (DFT) nor the quasiharmonic approximation (QHA) have been tested at these ultrahigh pressures and temperatures (*PT*s). Here, we use the Mermin functional (*7*), i.e., the finite electronic temperature (T_{el}) version of DFT that includes thermal electronic excitations, and ultrasoft pseudopotentials (*8*) based on orbitals with quantum number n = 2 and 3 for all three atoms. We studied $MgSiO_3$, MgO, and SiO_2 up to 80 Mbar and 20,000 K (figs. S1 and S2, A to C).

$MgSiO_3$ could transform to another ABX_3-type silicate or dissociate. We searched systematically for possible ABX_3 structures having likely high-pressure coordinations and connectivities, but found none with enthalpy lower than the $CaIrO_3$-type polymorph (see supporting online material). This phase dissociated into CsCl-type MgO and cotunnite-type SiO_2 at 11.2 Mbar in static calculations (Fig. 1). Both binary oxides undergo phase transitions below 11.2 Mbar. MgO undergoes the NaCl-type → CsCl-type transformation at 5.3 Mbar, and SiO_2 undergoes a series of phase transitions: stishovite → $CaCl_2$-type → α-PbO_2-type → pyrite-type → cotunnite-type at 0.48, 0.82, 1.9, and 6.9 Mbar, respectively (Fig. 2). Our static transition pressures agree well with previous first-principles results (*9–12*) and experimental transition pressures (*13*, *14*), except for the α-PbO_2-type → pyrite-type transition in SiO_2, which has been observed once at 2.6 Mbar (*15*). CsCl-type MgO and cotunnite-type SiO_2 have not yet been seen experimentally. Baddeleyite-type and OI-type phases occur as pre-cotunnite phases in TiO_2 (*16*), an analog of SiO_2. Our results show

[1]Department of Chemical Engineering and Materials Science and Minnesota Supercomputing Institute, University of Minnesota, 421 Washington Avenue SE, Minneapolis, MN 55455, USA. [2]Department of Physics and Astronomy, Stony Brook University, Stony Brook, NY 11794–3800, USA.

*To whom correspondence should be addressed. E-mail: wentzcov@cems.umn.edu

that, in agreement with previous calculations (*12*), these phases are metastable with respect to pyrite-type and cotunnite-type SiO_2. Phonon frequencies in the $CaIrO_3$-type phase and in the binary oxides increase with pressure. In our calculations, no soft phonons occurred up to 80 Mbar, the pressure at Jupiter's center. As expected, soft phonons occurred in CsCl-type MgO (~2 Mbar) and in cotunnite-type SiO_2 (~1.5 Mbar) upon decompression (fig. S2).

Thermal electronic excitations have negligible effect on the structural, vibrational, and thermal properties of these phases, even at 20,000 K, shifting the phase boundary by less than 1 GPa. Empirically, the QHA should work well until the thermal expansivity $\alpha(P,T)$ becomes nonlinear (*17*). We find linear T scaling up to the dashed lines in the phase diagram shown in Fig. 3A. The Clapeyron slope ($dP/dT = dS/dV$) of the dissociation has large negative values at most pressures: −18 MPa/K at 5000 K increasing to −33 MPa/K at 10,000 K. This is caused by an increase in the average bond lengths [2.91 to 3.08 atomic units (au) for Mg-O bond and 2.59 to 2.76 au for Si-O bond] across the dissociation as cation coordination numbers increase. This decreases the average phonon frequencies and increases the entropy (*18*). At the same time, there is a density increase of 1 to 3% (Fig. 3B; fig. S3 and table S2). Negative Clapeyron slopes occurred also for the NaCl-type to CsCl-type MgO and for the pyrite-type to cotunnite-type SiO_2. In both cases, cation coordination numbers and average bond lengths increase through the transition (3.10 to 3.33 au in NaCl-type → CsCl-type MgO; 2.81 to 2.90 au in pyrite-type → cotunnite-type SiO_2).

This dissociation should affect models of the gas giants' cores (Fig. 3). $CaIrO_3$-type $MgSiO_3$ cannot exist in the cores of Jupiter and Saturn, but should survive in the cores of Uranus and Neptune, unless another phase transition not identified yet occurs at lower pressures. In Jupiter and Saturn, the dissociation occurs at *PT*s typically expected within the metallic-hydrogen envelope. The importance of this transformation for terrestrial exoplanets is more striking. Super-Earth is predicted to have a temperature of at least ~4000 K and a pressure of ~10 Mbar at its CMB (*19*). This places the dissociation near its CMB. The eventual occurrence of this endothermic transition with a large negative Clapeyron slope just above its CMB would be similar to the occurrence of the endothermic postspinel transition near the core of Mars. Geodynamical modeling suggests that this might be the cause of a proposed large martian superplume (*20*). Convection in a Dense-Saturn planet could be dramatically affected. *PT*s in this planet should be higher than in Saturn's interior (Fig. 3), given its smaller size and higher surface *T*s. A transformation with such large negative Clapeyron slope in the middle of the silicate core/mantle of terrestrial planets is likely to inhibit convection (*21*), promote layering, and produce differentiated mantles/cores, with a lower layer consisting primarily of oxides.

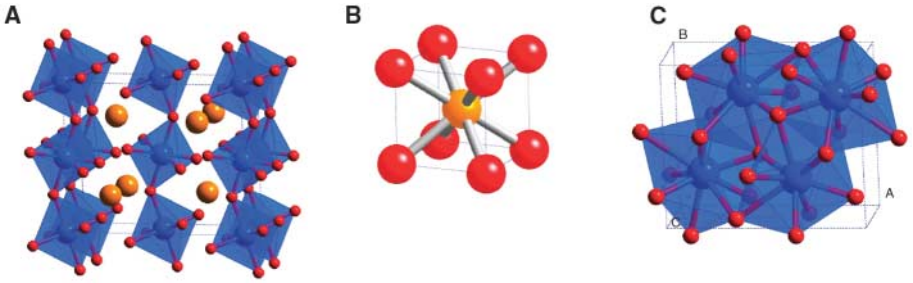

Fig. 1. Crystal structures of the stable phases. (**A**) $CaIrO_3$-type $MgSiO_3$ at static 10 Mbar. The space group is *Cmcm*. Lattice constants are (*a*, *b*, *c*) = (2.10, 6.42, 5.26) Å. Atomic coordinates are Mg(4c) (0, 0.749, 0.25), Si(4a) (0, 0, 0), O_1(4c) (0, 0.070, 0.25), and O_2(8f) (0, 0.353, 0.438). (**B**) CsCl-type MgO at static 12 Mbar. The space group is *Pm3m*. The lattice constant is a = 1.870 Å. (**C**) Cotunnite-type SiO_2 at static 12 Mbar. The space group is *Pbnm*. Lattice constants are (*a*, *b*, *c*) = (4.69, 3.95, 2.08) Å. Atomic coordinates are Si(4c) (0.141, 0.232, 0.25), O_1(4c) (0.435, 0.348, 0.25), and O_2(4c) (0.666, 0.984, 0.25).

Fig. 2. Differences between static enthalpies of aggregation of MgO and SiO_2 in various forms and $CaIrO_3$-type $MgSiO_3$. Dashed lines denote static transition pressures of NaCl-type → CsCl-type MgO, α-PbO_2-type → pyrite-type SiO_2, and pyrite-type → cotunnite-type SiO_2.

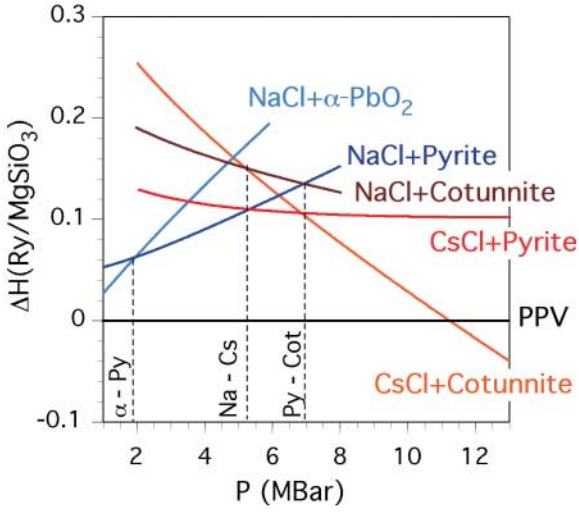

At *PT*s relevant for the giants and exoplanets, major changes in materials properties take place: These minerals become intrinsic semiconductors with electronic gaps (Fig. 4A). Local density approximation (LDA) usually underestimates band gaps by ~50%, whereas electron-phonon interactions cause gaps to narrow by a couple of eVs at elevated *T*s (*22*). The intrinsic carrier [electrons (n) and holes (p)] concentrations, in the range of 10,000 to 20,000 K (Fig. 4B), are typical of semimetals or heavily doped semiconductors. We focus on cotunnite-type SiO_2 with the largest carrier concentration.

In evaluating transport coefficients, we treat holes as immobile (*23*). This model is motivated by the relatively flat valence band edge of cotunnite-type SiO_2. Only thermal electrons are free and can carry both electrical and heat currents. The carrier density, n, from Fig. 4B can be represented by

$$n = 4\left(\frac{1}{V_c \lambda_{th}^3}\right)^{1/2} e^{-E_g/2k_BT} \qquad (1)$$

where the thermal wavelength is $\lambda_{th} = \sqrt{2\pi\hbar^2/m_e k_B T}$, and the cell volume V_c and effective mass m_e are 276 a_0^3 and 0.4m, with a_0 and m being the Bohr radius and the electron mass. Assuming that band gap E_g = 5 eV and taking $T = 10^4$ K, we obtain $n \approx 8 \times 10^{20}$ cm^{-3}; 0.9% of SiO_2 units have one excited electron and hole. This carrier density is typical of semimetals or heavily doped semiconductors.

The electrical conductivity, σ, is obtained from (*24*, *25*)

$$\sigma = ne\mu \text{ and } \mu = \frac{e\langle\tau\rangle}{m} \qquad (2)$$

where μ is the mobility and $\langle\tau\rangle$ is the average inverse scattering rate. There are three scattering mechanisms: (i) Coulomb scattering of carriers from each other; (ii) scattering from impurities or defects; and (iii) scattering by phonons, both Fröhlich (F) and optical deformation potential (*24*). Coulomb scattering is primarily electrons scattering from holes. Be-

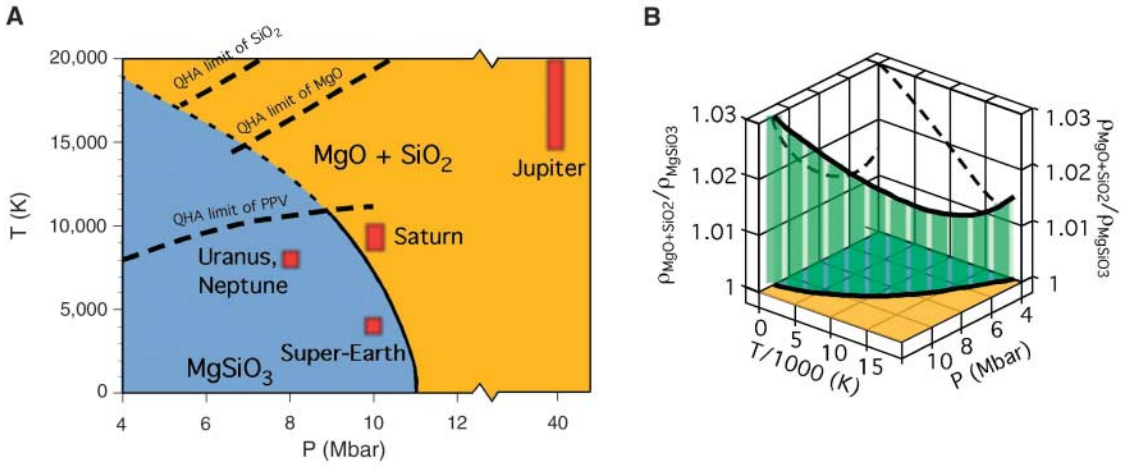

Fig. 3. (**A**) Pressure-temperature phase diagram showing the dissociation of $CaIrO_3$-type $MgSiO_3$ into CsCl-type MgO and cotunnite-type SiO_2. Red areas denote estimated pressure-temperature conditions at core-envelope boundaries in the solar giants and in Super-Earth. Dashed lines indicate the limit of validity of the quasiharmonic approximation (QHA). The dashed part of the phase boundary is more uncertain. (**B**) Density increase caused by the dissociation.

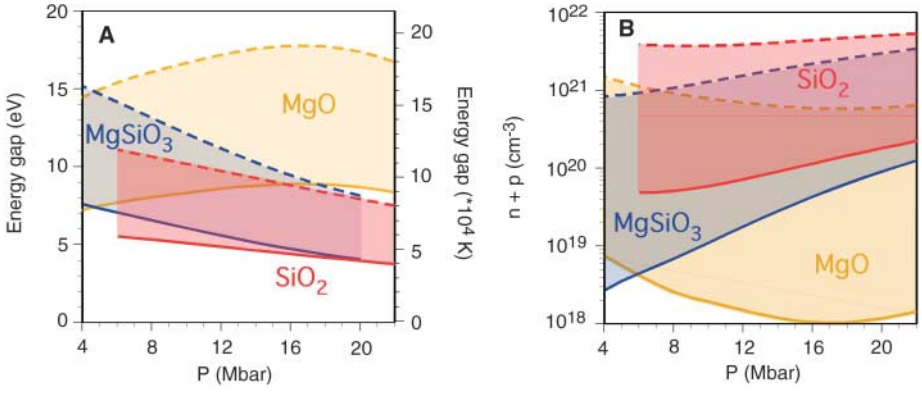

Fig. 4. (**A**) Solid and dashed lines denote the LDA band gaps of the phases involved, E_g^{LDA} and $2 \times E_g^{LDA}$, respectively. Actual band gaps should be in this range. (**B**) Total carrier (n = electrons, p = holes) concentration at 10,000 K (solid lines) ~ 20,000 K (dashed lines) assuming $E_g = 2 \times E_g^{LDA}$. This should be a lower bound for the carrier concentration.

cause holes are assumed to be localized, this is just a form of charged impurity scattering and likely weaker than scattering from impurities (Al, Fe, OH). Impurity and Fröhlich scattering suffer Debye-Hückel screening (*24*, *25*), with inverse screening length κ given by $\kappa^2 = \frac{4\pi n e^2}{\varepsilon_\infty k_B T}$. With our computed dielectric constant $\varepsilon_\infty \approx 4$, $1/\kappa \sim 4.7$ Å. We obtain the following estimates (see supporting online material):

$$\frac{\hbar}{\langle \tau_{DP} \rangle} = 0.07 \times \left(\frac{T}{10^4\ \mathrm{K}} \right)^{3/2} \mathrm{eV} \quad (3)$$

$$\frac{\hbar}{\langle \tau_{F} \rangle} = 0.08 \times \left(\frac{T}{10^4\ \mathrm{K}} \right)^{1/2} \mathrm{eV} \quad (4)$$

$$\frac{\hbar}{\langle \tau_{imp} \rangle} = 7.7 x_{imp} \times \left(\frac{T}{10^4\ \mathrm{K}} \right)^{-3/2} \mathrm{eV} \quad (5)$$

where x_{imp} is the fraction of Si atoms substituted by impurities of effective charge $Z = 1$. The Fröhlich and impurity rates have additional weak T-dependence (not shown) arising from temperature-dependent screening.

The ratio between impurity and electron-phonon scattering rates is $\frac{7.7 x_{imp}}{0.15} = 50 x_{imp}$, at $T = 10^4$ K. If more than 2% of Si atoms are replaced by charged impurities, impurity scattering dominates but falls rapidly at higher T. Minor element partitioning between MgO and SiO_2 at these conditions is unknown, and impurity centers may provide thermally inexpensive sources of new carriers. Therefore, any estimate of the influence of impurities has significant uncertainty. Ignoring impurity scattering, the electron-phonon scattering then gives an upper bound for the electronic mobility $\mu \sim 20$ cm²/V·s. This exceeds mobilities of typical metals (near 10 cm²/V·s at 300 K and falling as $1/T$) but is smaller than $\mu \sim 1400$ cm²/V·s for electrons in intrinsic Si at 300 K. The result is $\sigma \approx 2.6 \times 10^3$ (ohm·cm)$^{-1}$. The corresponding resistivity, $\rho \approx$ 380 microhm·cm, is only twice that of liquid iron at atmospheric pressure (*26*). We believe this is a reliable lower limit and that uncertainties (primarily the value of E_g, the concentration of charged impurity centers, and neglect of some weaker phonon-scattering processes) may increase the resistivity by less than a factor of 5 (see supporting online material). This would still leave the material essentially a metal!

The thermal conductivity can be estimated using an appropriate Weidemann-Franz ratio, $\kappa_{el}(T) = \left(\frac{2k_B^2 T}{e^2} \right) \sigma \approx 40$ W/mK. This is large compared to values of 2 to 4 W/mK that are representative of vibrational heat transport in hot anharmonic insulators (*27*). We also conclude that radiative heat transport should not be significant, despite the high energy content in the black-body spectrum at such high T. Because of free electrons (*28*), no photons propagate with frequencies less than the plasma frequency $\omega_p = \sqrt{4\pi n e^2 / \varepsilon_\infty m_e} \approx 0.9$ eV. Above this energy, electronic absorption from deep levels in the gap, resulting from structural defects or impurities, such as iron, is likely to limit the radiative term to values smaller than the electronic contribution. The conductivities, both thermal and electrical, of cotunnite-type SiO_2 and most oxides and silicates in terrestrial exoplanets will be large because of carriers activated over the insulating gap.

The dissociation of $CaIrO_3$-type $MgSiO_3$ stands as a challenge to be investigated by ultrahigh-pressure experiments. An alternative, low-pressure analog is $NaMgF_3$. This compound exists in the *Pbnm*-perovskite structure at ambient pressure and is predicted to transform to the postperovskite structure at 17.5 GPa and to dissociate into NaF (CsCl-type) and MgF_2 (cotunnite-type) at ~40 GPa, after the fluorides undergo transitions similar to those of the oxides (*29*). The postperovskite transformation appears to have been observed already (*30*), although the dissociation has not been observed yet.

References and Notes

1. M. Murakami *et al.*, *Science* **304**, 855 (2004).
2. T. Tsuchiya *et al.*, *Earth Planet. Sci. Lett.* **224**, 241 (2004).
3. A. R. Oganov, S. Ono, *Nature* **430**, 445 (2004).
4. E. J. Rivera *et al.*, *Astrophys. J.* **634**, 625 (2005).
5. B. Sato *et al.*, *Astrophys. J.* **633**, 465 (2005).
6. T. Guillot, *Phys. Today* **57**, 63 (2004).

7. D. Mermin, *Phys. Rev. B* **137**, A1441 (1965).
8. D. Vanderbilt, *Phys. Rev. B* **41**, 7892 (1990).
9. A. R. Oganov *et al.*, *J. Chem. Phys.* **118**, 10174 (2003).
10. B. B. Karki *et al.*, *Phys. Rev. B* **55**, 3465 (1997).
11. T. Tsuchiya *et al.*, *Geophys. Res. Lett.* **31**, L11610 (2004).
12. A. R. Oganov *et al.*, *Phys. Rev. B* **71**, 064104 (2005).
13. S. Ono *et al.*, *Earth Planet. Sci. Lett.* **197**, 187 (2002).
14. M. Murakami *et al.*, *Geophys. Res. Lett.* **30**, 1207 (2003).
15. Y. Kuwayama *et al.*, *Science* **309**, 923 (2005).
16. N. A. Dubrovinskaia *et al.*, *Phys. Rev. Lett.* **87**, 275501 (2001).
17. B. B. Karki *et al.*, *Science* **286**, 1705 (1999).
18. A. Navrotsky, *Geophys. Res. Lett.* **7**, 709 (1980).
19. D. Valencia, R. J. O'Connell, D. Sasselov, *Icarus,* in press.
20. S. A. Weinstein, *J. Geophys. Res.* **100**, 11719 (1995).
21. P. J. Tackley, *J. Geophys. Res.* **100**, 15477 (1995).
22. P. B. Allen, V. Heine, *J. Phys. C* **9**, 2305 (1976).
23. K. S. Song, R. T. Williams, *Self-Trapped Excitons* (Springer, Berlin, ed. 2, 1995), chap. 7.
24. J. M. Ziman, *Electrons and Phonons* (Oxford Univ. Press, London, 1960).
25. F. J. Blatt, *Physics of Electronic Conduction in Solids* (McGraw-Hill, New York, 1968).
26. R. S. Hixson *et al.*, *Phys. Rev. B* **42**, 6485 (1990).
27. G. A. Slack, in *Solid State Physics*, F. Seitz, D. Turnbull, Eds. (Academic Press, New York, 1980), vol. 34, pp. 1–71.
28. S. P. Clark Jr., *Trans. Am. Geophys. U.* **38**, 931 (1957).
29. J. Parise *et al.*, *Eos Trans. AGU* **85** (Fall Meet. Suppl.), abstr. MR23A-0188 (2004).
30. H.-Z. Liu *et al.*, *Geophys. Res. Lett.* **32**, L04304 (2005).

31. We thank D. Yuen, R. J. O'Connell, and D. Valencia for discussions and for sharing their unpublished results. Research was supported by NSF grants EAR-0135533, EAR-0230319, and ITR-0428774/ITR-0426757 (Virtual Laboratory for Earth and Planetary Material, a NSF-funded project at the Minnesota Supercomputing Institute; www.vlab.msi.umn.edu).

Supporting Online Material

www.sciencemag.org/cgi/content/full/311/5763/983/DC1
Methods
SOM Text
Figs. S1 to S4
Tables S1 and S2
References and Notes

3 October 2005; accepted 30 December 2005
10.1126/science.1120865

Changes in the Velocity Structure of the Greenland Ice Sheet

Eric Rignot[1]* and Pannir Kanagaratnam[2]*

Using satellite radar interferometry observations of Greenland, we detected widespread glacier acceleration below 66° north between 1996 and 2000, which rapidly expanded to 70° north in 2005. Accelerated ice discharge in the west and particularly in the east doubled the ice sheet mass deficit in the last decade from 90 to 220 cubic kilometers per year. As more glaciers accelerate farther north, the contribution of Greenland to sea-level rise will continue to increase.

The contribution of the Greenland Ice Sheet to sea level is a problem of considerable societal and scientific importance. Repeat-pass airborne laser altimetry measurements (*1*) showed that the ice sheet is nearly in balance in the interior but its periphery is thinning, with deterioration concentrated along the channels occupied by outlet glaciers (*2*). The most recent surveys revealed that the mass loss from the periphery is increasing with time, with approximately half of the increase caused by enhanced runoff and half by enhanced glacier flow (*3*).

Although these airborne surveys crisscrossed a large fraction of Greenland, they left major gaps in glacier coverage, particularly in the southeast and northwest. The mass loss from nonsurveyed glaciers was estimated using an ice melt model, thereby assuming no temporal changes in ice flow. If glacier dynamics is an important factor, the contribution to sea level from Greenland is underestimated using this approach. To address this issue and understand the exact partitioning between surface mass balance and ice dynamics, it is essential to estimate glacier discharge and its variability over time.

Here, we measure glacier velocities using satellite radar interferometry data collected by Radarsat-1 in fall 2000 (*4*, *5*) along the entire coast of Greenland except the southwest (Fig. 1) and repeatedly in spring and summer 2005 along selected tracks covering major glaciers. We also use European Remote Sensing satellites ERS-1 and ERS-2 data from winter 1996 in the north, east, northwest, and central west, and Envisat Advanced Synthetic Aperture Radar (ASAR) data from summer 2004 in the southwest. Ice velocity is measured with a precision of 10 to 30 m/year depending on satellite, data quality, and processing and is combined with ice thickness to calculate ice discharge.

Ice thickness is estimated with a precision of 10 m from airborne radio echo sounding data collected in 1997 to 2005 (*6*). Although grounding-line thicknesses of glaciers extending into floating ice tongues in the north are well known, ice thickness is difficult to measure at the fronts of calving glaciers in other parts of Greenland where no floating ice tongues develop. Ice thickness is only known several km upstream of the ice fronts. Ice fluxes are thus calculated at these upstream flux gates with a precision of 4%. Ice-front discharge is deduced from the upstream flux by subtracting a zero-anomaly surface mass balance (*7*) between the flux gate and the ice front. The correction is small (Table 1). Ice-front discharge is initially calculated for 1996 if data are available; otherwise, it is calculated for 2000. Ice-front discharge in subsequent years is obtained by multiplying the reference discharge by the percentage velocity increase averaged at the ice front, with a precision reduced to 10% because ice thickness is assumed to be steady. This approach alleviates the lack of frontal thickness data, accounts for higher dynamic losses nearer to the ice fronts, but omits dynamic losses below flux gates in the reference-year calculation. Mass loss for each glacier system is deduced from the ice-front discharge in excess of the zero-anomaly surface mass balance calculated for the entire drainage, with a precision of 14% (Table 1).

We examined the seasonal variability in flow speed of major glaciers in fall 2000. We found no velocity change from September to January at the 1% level over the 24-day averaging period of Radarsat-1. On the Petermann Glacier (1 in Fig. 1), a continuous set of observations in 2004 reveals an 8% increase in the summer months compared to winter (Fig. 2A). A similar seasonality is detected on Nioghalvfjerdsbrae and all southeast Greenland glaciers and has been observed on Jakobshavn Isbrae (*8*) and Columbia Glacier, Alaska (*9*). Winter velocities are therefore only 2% lower than the annual means, and flow changes must exceed 8% to be significant. No seasonal correction is applied to our data to compensate for the fact that surface velocities may represent 97 to 99% of vertically integrated velocities at the flux gates.

A nearly comprehensive estimate of ice discharge around Greenland is obtained for year 2000, and partial coverage for 1996 and 2005. The results are used to detect changes in ice discharge around the periphery caused by ice dynamics alone and determine their impact on ice sheet mass balance, independent of temporal changes in surface mass balance, i.e., accumulation and melt.

Many changes in velocity are observed in the north, but they are of little consequence to total mass balance. Harald Moltke Glacier was surging in 2005 after a quiescent phase. Nearby Tracy and Heilprin glaciers accelerated 40% and 18% in 2000 to 2005 (Fig. 2L), but the corresponding mass loss is small. Petermann Glacier has been stable since 1996, and its mass balance remains slightly negative. Academy Glacier tripled its speed in 2005 (Fig. 2C), which is typical for northern Greenland surge-type glaciers; its mass balance averages zero over the last decade. Farther east, the mass losses from decelerating Nioghalvfjerdsbrae and accelerat-

[1]Jet Propulsion Laboratory, California Institute of Technology, Mail Stop 300-319, Pasadena, CA 91109–8099, USA. [2]Center for Remote Sensing of Ice Sheets (CReSIS), University of Kansas, Lawrence, KS 66045, USA.

*To whom correspondence should be addressed. E-mail: eric.rignot@jpl.nasa.gov (E.R), pannir@ku.edu (P.K.)